

# Relationship of Band-Edge Luminescence to Recombination Lifetime in Silicon Wafers

R.K. AHRENKIEL,<sup>1,2,3</sup> S.W. JOHNSTON,<sup>2</sup> W.K. METZGER,<sup>2</sup> and P. DIPPO<sup>2</sup>

1.—Departmental of Metallurgical and Materials Engineering, Colorado School of Mines, Golden, CO, USA. 2.—National Renewable Energy Laboratory, Golden, CO, USA. 3.—e-mail: rahren@mac.com

In recent years, intrinsic luminescence has been used as a method to characterize the recombination lifetime of crystalline silicon. The assumption is that the steady-state intrinsic photoluminescence at 1.09 eV (1.134  $\mu\text{m}$ ) can be related to the recombination lifetime. In this work, we measured the band-edge photoluminescence (PL) intensities of a number of single-crystal wafers. The resistivity in the wafer set ranges from 1 to 11,000 ohm-cm under constant excitation intensity. We then measured the PL spectra and recombination lifetimes of these wafer sets under a variety of conditions. The lifetime was measured using resonant-coupled photoconductive decay (RCPD) in both air ambient and an iodine/methanol solution. The same procedure was used for the PL spectra. Plots of the measured lifetime versus the PL intensity showed weak correlation between the two quantities in air ambient. However, there is a positive relationship between the near-bandgap PL intensity and the recombination lifetime for passivated surfaces. Some fundamental physical reasons will be used to explain these results.

**Key words:** Silicon, recombination lifetime, minority carrier lifetime, photoluminescence

## INTRODUCTION

Recombination lifetime analysis is critically important in photovoltaic and other electronic technologies. Improved methods of lifetime characterization are an area of intense research activity. Silicon is the primary material used in current, commercial photovoltaic technology. The standard methods for measuring recombination lifetime in silicon involve several experimental configurations that measure the photoconductive decay rate. These include transient microwave reflection<sup>1</sup> and the quasi-static technique.<sup>2</sup> Several research groups<sup>3–9</sup> have recently used photoluminescence (PL) spectra as a diagnostic in multicrystalline silicon. The silicon band-edge PL intensity is taken as related to the carrier lifetime in much of the cited work. Here, we

will examine this relationship on single-crystal materials that have a wide range of doping densities, and assess the technique as an indicator of carrier lifetime.

Because silicon is an indirect-bandgap semiconductor, the internal quantum efficiencies are extremely small by comparison with direct-bandgap materials such as GaAs. The intrinsic radiative recombination or B-coefficient in silicon is  $2 \times 10^{-15} \text{ cm}^3/\text{s}$ ,<sup>10</sup> which is about  $10^{-5}$  times less than that of GaAs.<sup>11</sup> Consequently, measurements have produced absolute quantum efficiencies for silicon that vary from  $10^{-6}$  to  $10^{-4}$ . Hence, radiative recombination at defects is accentuated because of the localized absence of translational symmetry and the small band-edge PL intensity. For example, significantly larger (5%) quantum efficiencies have been observed due to PL generated at very deep sulfur and selenium defects.<sup>12</sup> The majority of the defect-produced PL, which arises from the common donor/acceptor species such as

(Received March 6, 2007; accepted October 12, 2007; published online November 14, 2007)

phosphorous and boron, occurs near the band-to-band luminescence. These transitions are commonly seen at 4 K, as excitons that bind to various defects and have unique emission lines. At low temperature, PL spectroscopy is used as a means of defect identification.<sup>13</sup> At room temperature, these PL emissions broaden and the individual components cannot usually be distinguished.

### TRANSPORT PROPERTIES

The bulk quantum efficiency of any semiconductor can be written as:

$$\eta = \frac{R_r}{R_r + R_{nr}} = \frac{\tau_{nr}}{\tau_{nr} + \tau_r}. \quad (1)$$

Here,  $R_r$ ,  $R_{nr}$  are the radiative and nonradiative recombination rates, and  $\tau_r$ ,  $\tau_{nr}$  are the respective lifetimes. In low-injection conditions, the radiative lifetime is given by:

$$\tau_r = \frac{1}{BN}, \quad (2)$$

where  $B$  is the intrinsic radiative recombination coefficient, which is about  $2 \times 10^{-15} \text{ cm}^3/\text{s}$  for silicon, as noted earlier.  $N$  is the doping or majority-carrier density. Therefore, at a doping density of  $1 \times 10^{17} \text{ cm}^{-3}$ , the radiative lifetime is about 50 ms and is orders of magnitude larger than the typical Shockley–Read–Hall<sup>14,15</sup> lifetime. Therefore, the bulk quantum efficiency can be expressed as:

$$\eta = BN\tau_{nr}. \quad (3)$$

Equation 3 indicates that the bulk PL intensity is a product of the doping density and the nonradiative lifetime.

### Effect of Surfaces

In most silicon wafers of standard thickness (i.e., 300  $\mu\text{m}$ ), the unpassivated surface is a strong component of the nonradiative recombination. To determine the effects of surface recombination on the PL intensity, one must solve the drift-diffusion equations with both bulk and surface components being present. The solution to this problem for an infinitely thick crystal has been developed in the literature<sup>16</sup>:

$$\eta = \frac{BN\tau_{nr}}{1 + SL/D} \left( 1 + \frac{SL/D}{1 + \alpha L} \right). \quad (4)$$

Here,  $S$  is the front-surface recombination velocity;  $L$  and  $D$  are the minority-carrier diffusion length and diffusivity, respectively; and  $\alpha$  is the absorption coefficient of the incident monochromatic light. At  $S = 0$ , Eq. 4 reduces to Eq. 3 and only the bulk lifetime and concentration influence the PL efficiency. Equation 3 is also valid when the thickness of the wafer is much larger than the diffusion length  $L$ . When these conditions do not hold, one

can use an approximate expression<sup>17</sup> for the surface lifetime component:

$$\tau_s = \frac{d}{2S} + \frac{d^2}{\pi^2 D}. \quad (5)$$

Here,  $d$  is the sample thickness and  $\tau_s$  is the surface contribution to the nonradiative lifetime. The total nonradiative lifetime becomes:

$$\frac{1}{\tau_{nr}} = \frac{1}{\tau_s} + \frac{1}{\tau_b}. \quad (6)$$

This expression can be combined with Eqs. 5 and 3 to give the total quantum efficiency,

$$\eta = \frac{BN}{\frac{1}{\tau_b} + \frac{d}{2S} + \frac{d^2}{\pi^2 D}}. \quad (7)$$

In summary, the drift-diffusion equations indicate that the quantum efficiency, or PL intensity, is only proportional to the product of the bulk lifetime and the carrier concentration (Eq. 3) when the surface-recombination velocity is very small.

Using Eq. 7, we calculated the internal quantum efficiency ( $\eta$ ) of the PL using bulk, nonradiative lifetime as the variable parameter. The surface-recombination velocity is taken as an independent parameter. In Fig. 1, we simulated an excitation wavelength of 632 nm, which was the wavelength used in our laboratory for the experimental data that will be presented. We modeled a  $p$ -type wafer doped to a level of  $1 \times 10^{16} \text{ cm}^{-3}$ , and with a minority electron diffusivity of  $25 \text{ cm}^2/\text{s}$ . Curves A, B, and C correspond to front-surface recombination velocities of  $1$ ,  $1 \times 10^3$ , and  $1 \times 10^5 \text{ cm/s}$ , respectively. In the plot, Curve A shows a linear rela-

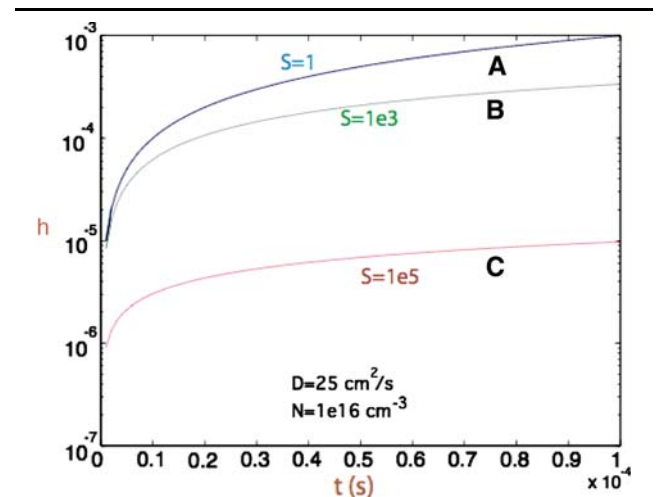


Fig. 1. Simulation of the quantum efficiency for a  $p$ -type silicon wafer doped  $1 \times 10^{16} \text{ cm}^{-3}$ , with a minority electron diffusivity of  $25 \text{ cm}^2/\text{s}$ . The wafer is assumed to have infinite thickness. Curves A, B, and C correspond to front-surface recombination velocities of  $1$ ,  $1 \times 10^3$ , and  $1 \times 10^5 \text{ cm/s}$ , respectively. An excitation wavelength of 632.8 nm is used in the simulations.

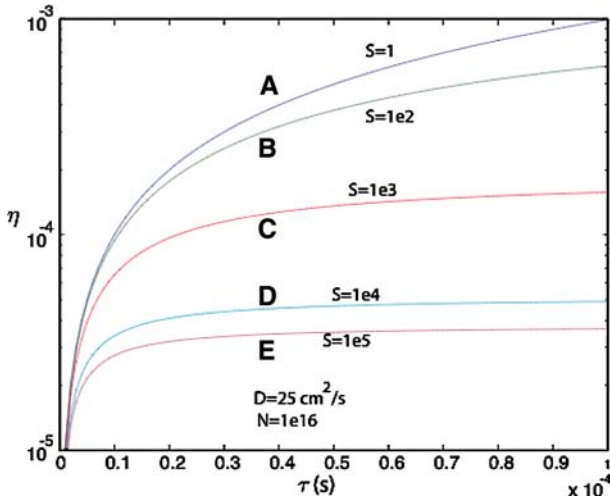


Fig. 2. Simulated quantum efficiency of a  $p$ -type wafer that is  $300\text{ }\mu\text{m}$  thick and boron-doped to  $1 \times 10^{16}\text{ cm}^{-3}$ . Curves A through E simulate front- and rear-surface recombination velocities varying from  $S = 1\text{ cm/s}$  (A) to  $S = 1 \times 10^5\text{ cm/s}$  (E). The electron diffusivity is fixed at  $25\text{ cm}^2/\text{s}$  in the calculations.

tionship between  $\eta$  and the bulk lifetime. When  $S = 10^3$  and  $10^5\text{ cm/s}$ ,  $\eta$  partially saturates at  $20\text{ }\mu\text{s}$  and  $30\text{ }\mu\text{s}$ , respectively.

For samples of finite thickness, we chose a  $p$ -type wafer that is  $300\text{ }\mu\text{m}$  thick and again doped to  $1 \times 10^{16}\text{ cm}^{-3}$ . In Fig. 2, curves A through E simulate front- and rear-surface recombination velocities varying from  $S = 1\text{ cm/s}$  to  $S = 1 \times 10^5\text{ cm/s}$ . For curves D and E, the efficiency completely saturates in the range of  $10\text{ }\mu\text{s}$  to  $20\text{ }\mu\text{s}$ . For curve C, the saturation occurs at about  $40\text{ }\mu\text{s}$ . For curve B, the efficiency deviates from the bulk lifetime value at lifetimes larger than  $10\text{ }\mu\text{s}$ , and the variation increases with increasing lifetime. Of course, curve A ( $S = 1$ ) on a linear scale again shows that  $\eta$  is proportional to  $\tau$  for the entire range of values.

In summarizing this section, we see that surface recombination is a significant factor in simulating the PL of unpassivated wafers. We will investigate these effects further by comparing the experimental PL-lifetime relationships in a series of passivated and unpassivated wafers.

### Resonance-Coupled Photoconductive Decay

The resonant-coupled photoconductive decay (RCPCD) technique<sup>18–21</sup> was used for measuring carrier lifetime in silicon and other semiconducting materials. Our system is a pump-probe technique, using an optical pump and a high-frequency probe. However, we use lower microwave frequencies ( $400\text{--}900\text{ MHz}$ ), which completely penetrate most wafers with common doping levels. This allows depth probes of wafers of standard ( $300\text{--}400\text{ }\mu\text{m}$ ) wafer thickness by using the longer optical excitation wavelengths. The RCPCD method is very linear in sample conductivity, and one can measure a linear response over more than three orders of magnitude

of carrier concentration. This attribute allows us to measure the carrier recombination lifetime over many decades of injection level. The RCPCD has been used on numerous samples, ranging from small-area thin films to  $300\text{-}\mu\text{m}$ -thick, 6-inch-diameter silicon wafers. Because the measurement system is contactless, samples may be placed in a passivating solution such as iodine/methanol.<sup>22</sup>

### Experimental Results

The wafers in these studies were obtained from a number of commercial sources. These included both wafer manufacturing companies and electronic companies that use similar wafers in their products. They were grown by both the Czochralski (CZ) and float-zone (FZ) methods. These were chosen to provide a cross section of materials used in the microelectronics and photovoltaic industries. Table I shows the wafer numbers, growth technique, and doping densities measured by the capacitance-voltage technique. Note that for some wafers, the growth technique was not known.

In Fig. 3, we show RCPCD low-injection data for wafers numbered 269–274 with characteristics shown in the table. These wafers were grown by various techniques and were obtained from six different wafer sources. The measurements were made in both air ambient and iodine/methanol passivating solution. This subset of wafers was boron-doped  $p$ -type over the range  $5 \times 10^{15}\text{ cm}^{-3}$  to  $2 \times 10^{16}\text{ cm}^{-3}$ . We see from the data that all unpassivated samples had effective lifetimes below  $10\text{ }\mu\text{s}$ . However, the passivated data showed lifetimes ranging from  $61\text{ }\mu\text{s}$  to  $77\text{ }\mu\text{s}$  on three of the wafers. These data show the strong effects of surface recombination on

Table I. Growth Technique and Doping Density for Wafer Samples

Wafer No.	Growth Technique	Doping Density ( $\text{cm}^{-3}$ )
23	CZ	$1.90 \times 10^{16}$
24	CZ	$1.69 \times 10^{16}$
25		$7.81 \times 10^{13}$
27	CZ	$3.38 \times 10^{14}$
28		$6.19 \times 10^{15}$
30		$5.50 \times 10^{16}$
31		$8.73 \times 10^{15}$
32	FZ	$4.85 \times 10^{16}$
33		$4.00 \times 10^{15}$
34	FZ	$6.93 \times 10^{16}$
35	FZ	$7.56 \times 10^{16}$
36	FZ	$3.63 \times 10^{15}$
37	CZ	$5.67 \times 10^{15}$
269	CZ	$1.90 \times 10^{16}$
270	FZ	$7.56 \times 10^{16}$
271		$4.00 \times 10^{15}$
272		$1.69 \times 10^{16}$
273	CZ	$5.67 \times 10^{15}$
274	FZ	$3.63 \times 10^{15}$

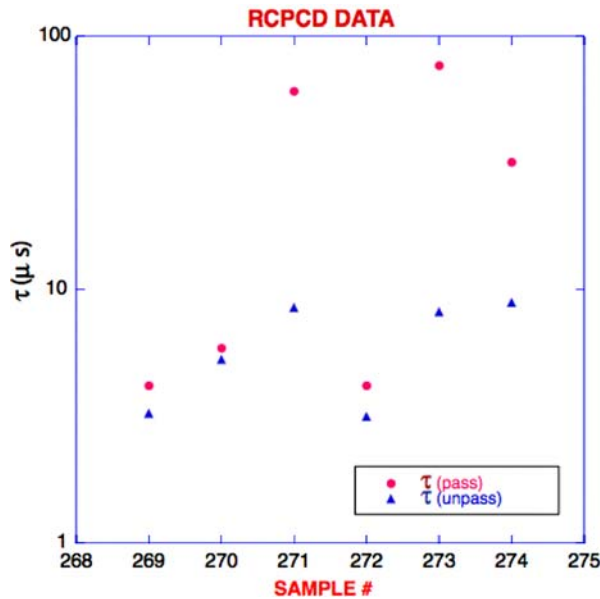


Fig. 3. The low-injection electron lifetime in a set of six single-crystal wafers obtained from six different wafers sources. These had  $p$ -type doping varying from  $5 \times 10^{15} \text{ cm}^{-3}$  to  $2 \times 10^{16} \text{ cm}^{-3}$ . The (circular) points are for measurements made in passivating iodine-methanol solution. The triangular points are the same samples made in air ambient. The lifetimes were measured by resonant-coupled photoconductive decay.

lifetime measurements. For unpassivated wafers, the surface recombination masks the bulk lifetime, and one cannot distinguish bulk wafer quality based on these measurements. Calculations of the effective recombination velocity may be performed from these data. The effective  $S$ -values ranged from 375 cm/s to 2849 cm/s on this sample set.

### PL Spectra

The PL data were obtained from a system with an optical multi-channel analyzer (OMA) and two different detector arrays. The first is a silicon-based charge-coupled device (CCD), and the second is an InGaAs array that extends the sensitivity into the infrared region. Several different continuous-wave (cw) lasers are available as excitation sources, and the chosen laser beam is modulated with a mechanical chopper. The latter allows the subtraction of dark current from the photocurrent by the associated electronics. A variable-temperature optical cryostat is used to cool the sample to as low as 4.2 K. We also added a sample holder that can contain a passivating liquid for room-temperature measurements with passivated surfaces. The measurements reported here were primarily made using a HeNe 632.8-nm cw laser, with an unattenuated power of 18 mW.

### Low-Temperature PL Spectra

The data of Fig. 4 were obtained by cooling three silicon wafers to 4.2 K and measuring the emission spectra with the InGaAs array detector. Sample 23

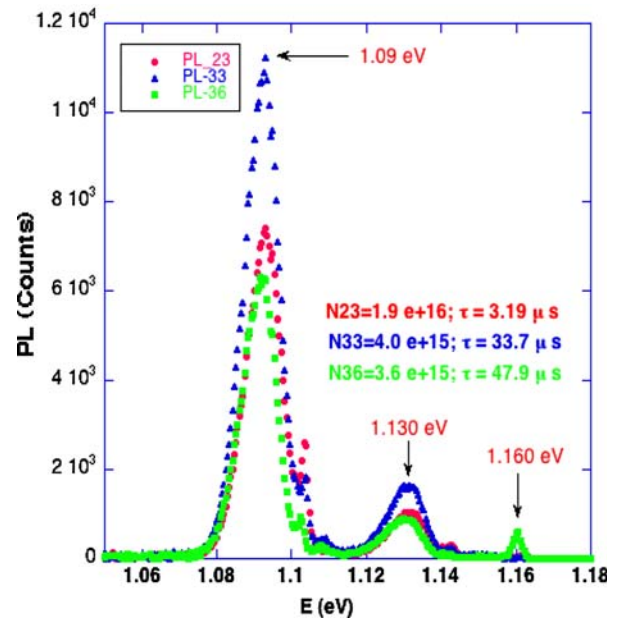


Fig. 4. Sample 23 is CZ-grown  $p$ -type wafer doped at  $1.6 \times 10^{16} \text{ cm}^{-3}$ . Sample 33 is a CZ-grown  $p$ -type wafer doped to  $4 \times 10^{15} \text{ cm}^{-3}$ . Sample 36 is a float-zone-grown,  $p$ -type wafer doped to  $3.6 \times 10^{15} \text{ cm}^{-3}$ . The measurements were made at 4.2 K.

is a CZ-grown  $p$ -type wafer that is boron-doped to a level of  $1.6 \times 10^{16} \text{ cm}^{-3}$ . The room-temperature, low-injection lifetime in iodine/methanol solution is 3.2  $\mu\text{s}$ . Sample 33 is a CZ-grown wafer doped  $p$ -type to a level of  $4 \times 10^{15} \text{ cm}^{-3}$ , and sample 36 is a float-zone-grown wafer doped  $p$ -type to a level of  $3.6 \times 10^{15} \text{ cm}^{-3}$ . The dominant feature in all three spectra is the boron-bound exciton (TO phonons) transition at about 1.09 eV. Because of the limited wavelength resolution of the OMA, we are likely seeing both TO,  $m = 1$  and TO,  $m = 2$  modes (1.0930 eV and 1.0909 eV, respectively) merged into one peak. The second peak at 1.13 eV is the free exciton peak, activated by the TA phonon. Finally, the free exciton peak at  $\sim 1.16$  eV is observed in very high-purity material; here, it is apparent only in the float-zone sample #36. Although the lifetime varies by more than an order of magnitude in these three samples, we see very little evidence of lifetime effects in the low-temperature spectral intensity. Plotting the  $N^*\tau$  product of these samples versus the amplitude of the boron-bound exciton produces no observable correlation. The free exciton band is only observable in the longer-lifetime, float-zone-grown sample. The latter result is probably the best correlation of high-lifetime and low-temperature spectral properties.

### Room-Temperature PL Spectra

The remainder of the work here will focus on room-temperature PL spectra. These data were all obtained using the silicon CCD array detector. This detector has been the basis for most of the current PL-lifetime correlation work.

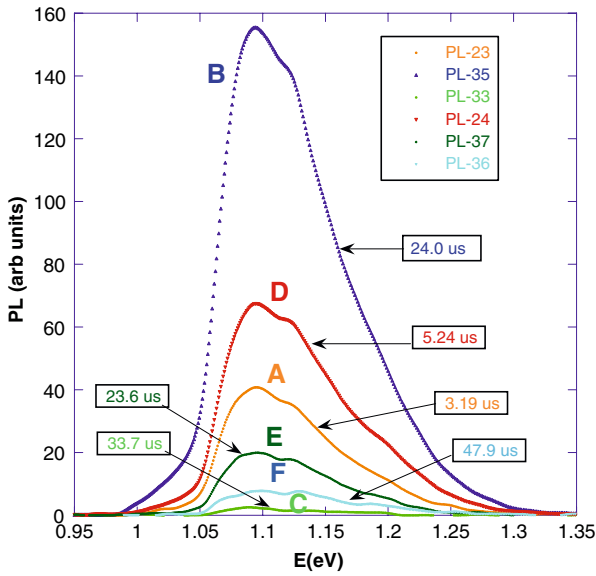


Fig. 5. The room-temperature PL spectra of six single-crystal wafers using the 632.8-nm excitation wavelength. The RCPCD lifetimes measured in passivating iodine-methanol solution are also indicated.

Figure 5 shows the room-temperature PL spectra of six samples from a variety of sources. The spectra were obtained using a constant excitation-intensity setting for the HeNe (632.8-nm) laser, and there is a large variation in PL intensity. The boron doping levels varied from  $3.6 \times 10^{15} \text{ cm}^{-3}$  to  $7.5 \times 10^{16} \text{ cm}^{-3}$  in this sample set. There is structure in the PL spectra, especially on the high-energy side of the bandgap (1.11 eV). These PL data were not normalized to the background doping. The low-injection minority-carrier lifetimes were measured by RCPCD in a passivating, iodine-methanol solution and are shown in the boxes. The weakest PL signal is found in sample 33, which has a lifetime of 33.7  $\mu\text{s}$ . The doping level of this sample is  $4.0 \times 10^{15} \text{ cm}^{-3}$ . The strongest PL signal is found in sample 35, which has a lifetime of 24.0  $\mu\text{s}$  and a doping level of  $7.5 \times 10^{16} \text{ cm}^{-3}$ . We see from these data that the PL intensity, without carrier concentration normalization, is not a reliable indicator of bulk lifetime.

Figure 6 shows a bar graph in which the passivated lifetime is plotted alongside the integrated PL intensity divided by the doping concentration for the same data shown in Fig 5. There is a correlation between the two parameters, but a considerable amount of scatter. Figure 7 is a plot with the unpassivated lifetime plotted versus the integrated PL intensity divided by the doping density. The correlation is slightly better, but there is still a considerable amount of scatter.

We see in Fig. 5 that there is considerable structure in the PL spectra, and several underlying transitions are present. These bands are impurity-related transitions that overlap the intrinsic band-to-band transition. These transitions distort the

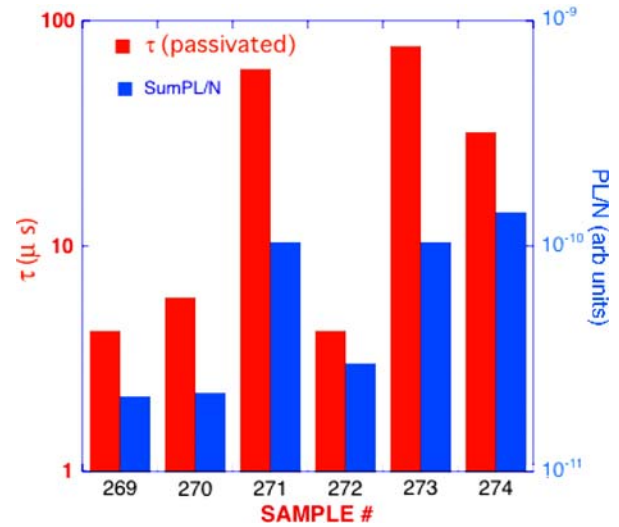


Fig. 6. Comparison of the recombination lifetime of passivated single-crystal wafers and the integrated PL intensity divided by the doping density. There were six samples used in this study and the complete spectra are shown in Fig. 5.

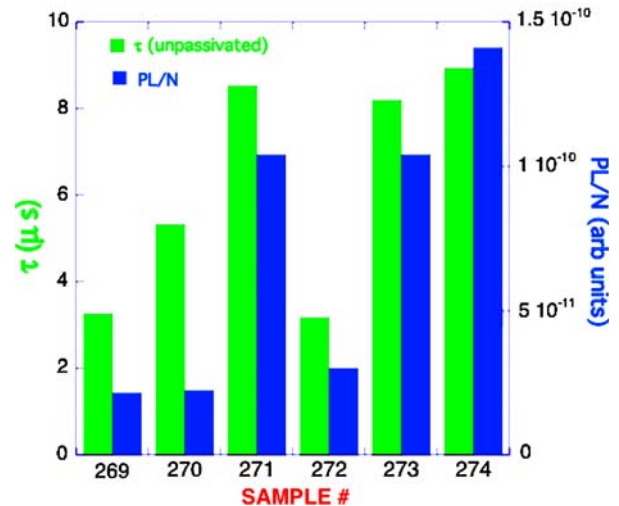


Fig. 7. Comparison of the recombination lifetime of unpassivated single-crystal wafers and the integrated PL intensity divided by the doping density. There were six samples used in this study and the complete spectra are shown in Fig. 5.

relationship between PL and lifetime and are one source of scatter seen in the data. Surface recombination effects also contribute to the scatter, as was shown in Figs. 1 and 2. Variations in the surface-recombination velocity from sample to sample influence the strength of the PL signal and add to the distortion of the relationship between integrated PL and lifetime.

In summary, we see that there is a correlation between the PL intensity and carrier-concentration-minority-carrier lifetime product. The correlation shows a positive trend, but the scatter is too large for accurate determination of carrier lifetime.



### PL in Iodine-Methanol Solution

We have measured a larger set of samples in a horizontal sample holder that allows PL measurement in passivating iodine-methanol solution. The same excitation intensity was used as for the samples measured in air. However, there were two additional loss mechanisms introduced here. There is attenuation of the incident laser beam and of the PL signal by absorption of the solution. The PL collection efficiency is lowered because of losses at additional optics required to divert the beam into the horizontal sample chamber.

The spectra of three samples are shown in Fig. 8. Sample 36 is a float-zone sample that is boron-doped to a level of  $3.63 \times 10^{15} \text{ cm}^{-3}$ . The passivated lifetime, as measured by RCPCD, is  $47.9 \mu\text{s}$ , and the unpassivated lifetime is  $8.9 \mu\text{s}$ . Curve A is the spectra in solution and curve B is the spectra in air. The ratio of the area of spectra A/B is 1.33, whereas the ratio of the respective lifetimes is 5.4. The difference is likely due, in part, to the optical loss in the solution. Sample 25 is an undoped float-zone sample with a passivated lifetime of  $455 \mu\text{s}$ . The background carrier concentration is about  $1 \times 10^{12} \text{ cm}^{-3}$  as measured by a four-point probe. The PL spectra of the passivated and unpassivated samples are shown in curves C and D, respectively. The integrated PL ratio is 12 and is again less than the respective lifetime ratios. Sample 23 is a CZ-grown sample boron-doped to  $1.8 \times 10^{16} \text{ cm}^{-3}$  and has a passivated lifetime of  $3.2 \mu\text{s}$ . The lifetime is unchanged in air ambient, indicating that the bulk defects completely dominated the lifetime. Curve E is measured in solution and curve F is measured in air. The integrated PL of the latter is about 2.4

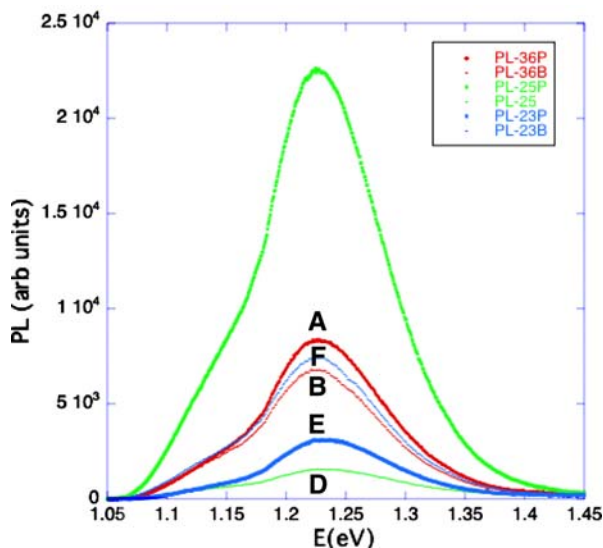


Fig. 8. The PL spectra of three samples measured in air and in a passivating iodine-methanol solution. Curves A and B are data from a float-zone-grown sample that is boron-doped to a level of  $3.63 \times 10^{15} \text{ cm}^{-3}$ . Curves C and D are data from a float-zone sample that is undoped and with a background doping of  $2 \times 10^{12} \text{ cm}^{-3}$ .

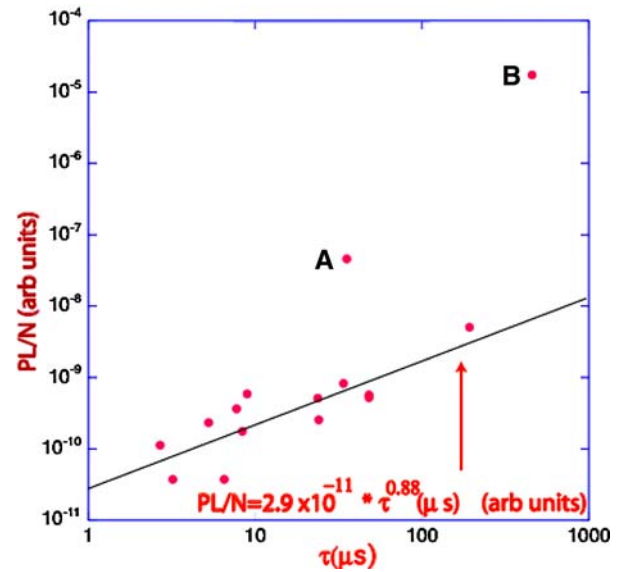


Fig. 9. The integrated band-edge PL of eight single-crystal wafers in iodine-methanol solution versus the passivated lifetime. The integrated PL intensity is divided by the doping density. The two outlying points A and B come from undoped and very high-resistivity float-zone wafers and are not included in the data fit. The PL increase is caused by high injection. There is a near-linear dependence of PL/N on the carrier lifetime. However, scatter is still a significant problem.

times that of the former. This difference is caused by the optical absorption of the solution measurement, because the lifetime ratio is nearly equal for this particular sample.

Eight samples were subjected to a similar analysis, and the data are summarized in Fig. 9. The doping ranged from  $2 \times 10^{12} \text{ cm}^{-3}$  to  $8 \times 10^{16} \text{ cm}^{-3}$ . The carrier concentration in each sample was measured by both a mercury probe and a four-point probe. The PL spectra were measured in the horizontal holder in iodine-methanol solution. The lifetimes were measured by RCPCD in iodine-methanol solution after a cleaning sequence, starting with an HF etch.

The lifetime versus integrated PL divided by carrier concentration are shown in Fig. 9. We show a power law fit of the  $\tau$  versus PL/N data. The high-resistivity samples were excluded from the fit, because calculations indicated that high-injection conditions were generated by the excitation source. The fit shows that PL/N increases with  $\tau^{0.88}$ , but there is a significant scatter about the fitting curve. The data show that PL/N is a qualitative indicator of carrier lifetime when the sample surfaces are passivated. The scatter is such as to make unreliable the quantitative determination of lifetime from PL intensity.

### DISCUSSION OF RESULTS

Our data show that PL intensity is not a reliable indicator of carrier lifetime unless the samples are passivated. This situation parallels that found for

the common techniques that measure lifetime by photoconductive decay. However in this work, there is a considerable amount of scatter in the data even when the sample is passivated during the PL measurement.

We see from the spectral data that the near-bandgap region contains overlapping peaks in addition to the intrinsic PL. These additional peaks are attributed to impurity transitions. These effects are more pronounced in silicon because of the weak transition probability of the indirect band-to-band process, which requires phonon assistance. Impurities disrupt local translational symmetry and relax the radiative selection rules. Therefore, the relative strength of impurity transitions is larger in silicon than in direct-bandgap materials. The overlap of impurity-activated transitions with the intrinsic band-to-band transition is a primary source of the scatter seen here. In the case of unpassivated surfaces, the near-bandgap impurity-activated transitions may become stronger than the intrinsic recombination band. The latter is weakened by strong recombination at surfaces as shown in Figs. 1 and 2. Because the radiating impurity is a competitive pathway to electron-hole recombination, the PL intensity will be inversely proportional to recombination lifetime in this process. Hence, there is a great deal of scatter in the PL-lifetime data in this case.

The surface recombination influences the PL measurement, as it does the photoconductive measurements. Thus, one must perform surface passivation to obtain reliable data.

In summary, room-temperature silicon PL luminescence should be a useful tool for qualitative analysis in silicon diagnostics, but it is not a reliable measurement tool for minority-carrier lifetime.

### ACKNOWLEDGEMENTS

The first author (RKA) would like to acknowledge the support of the Denver Research Institute and

the support of NREL under Subcontract #AAX-6-66011-01.

### REFERENCES

1. M. Kunst and G. Beck, *J. Appl. Phys.* 60, 3558 (1986).
2. R.A. Sinton and A. Cuevas, *Appl. Phys. Lett.* 69, 2510 (1996).
3. T. Trupke and R.A. Bardos, *Appl. Phys. Lett.* 85, 3611 (2004).
4. T. Trupke, R.A. Bardos, and M.D. Abbott, *Appl. Phys. Lett.* 87, 184102 (2005).
5. T. Trupke, R.A. Bardos, M.C. Schubert, and W. Warta, *Appl. Phys. Lett.* 89, 044107 (2006).
6. I. Tarasov, S. Ostapenko, C. Haessler, and E.-U. Reisner, *Mater. Sci. Eng.* B71, 51 (2000).
7. Y. Koshka, S. Ostapenko, I. Tarasov, S. McHugo, and J.P. Kalejs, *Appl. Phys. Lett.* 74, 1555 (1999).
8. S. Ostapenko, et al., *Semicond. Sci. Technol.* 15, 840 (2000).
9. J.P. Kalejs (DOE Solar Program Review Meeting 2004, DOE/GO-102005-2067, 2004) p. 173.
10. J.I. Pankove, *Optical Processes in Semiconductors* (New York: Dover Publications Inc., 1971), p. 111.
11. R.K. Ahrenkiel, B.M. Keyes, G.B. Lush, M.R. Melloch, M.S. Lundstrom, and H.F. MacMillan, *J. Vac. Sci. Technol. A* 10, 990 (1992).
12. O. King and D.G. Hall, *Phys. Rev. B* 10661 (1994).
13. EMIS Data Review, Series No. 4, *Properties of Silicon* (London: INSPEC, IEE, 1988).
14. W. Shockley and W.T. Read, *Phys. Rev.* 87, 335 (1952).
15. R.N. Hall, *Phys. Rev.* 87, 387 (1952).
16. R.K. Ahrenkiel, *Current Topics in Photovoltaics*, vol. 3, ed. T. Coutts and J. Meakin (New York: Academic Press, 1988), pp. 19–21.
17. R. K. Ahrenkiel, *Minority Carriers in III–V Semiconductors: Physics and Applications*, p. 83, *Semiconductors and Semimetals*, vol. 39, ed. R.K. Ahrenkiel and M.S. Lundstrom (Boston: Academic Press, 1993).
18. R.K. Ahrenkiel, *AIP Conference Proceedings*, vol. 394 (AIP Press, 1997), p. 225.
19. R.K. Ahrenkiel and S. Johnston, *Materials Research Society Symposium Proceedings*, vol. 510 (Materials Research Society, 1998), pp. 575–581.
20. R.K. Ahrenkiel and S.W. Johnston, *Mater. Sci. Eng.* B102, 161 (2003).
21. R. Ahrenkiel, U.S. patent 5,929,652 (27 July 1999); R. Ahrenkiel and S. Johnston, U.S. patent 6,275,060 (August 14, 2001); S. Johnston and R. Ahrenkiel, U.S. patent 6,369,603 (April 9, 2002).
22. H. M'Saad, J. Michel, J.J. Lappe, and L.C. Kimerling, *J. Electron. Mater.* 23, 487 (1994).